Electronic and crystal structure changes induced by in-plane oxygen vacancies in multiferroic YMnO_{3}

Shaobo Cheng, Menglei Li, Qingping Meng, Wenhui Duan, Y. G. Zhao, X. F. Sun, Yimei Zhu, and Jing Zhu

Electronic and crystal structure changes induced by in-plane oxygen vacancies in multiferroic YMnO$_3$

Shaobo Cheng[1], Menglei Li[2,3], Qingping Meng[4], Wenhui Duan[2], Y.G.Zhao[2], X.F.Sun[5,6,7],

Yimei Zhu[4], Jing Zhu[1,*]

[1] National Center for Electron Microscopy in Beijing, School of Materials Science and Engineering, The State Key laboratory of New Ceramics and Fine Processing, Key Laboratory of Advanced Materials (MOE), Tsinghua University, Beijing 100084, P. R. China

[2] Department of Physics and State Key Laboratory of Low-Dimensional Quantum Physics, Tsinghua University, Beijing 100084, P. R. China

[3] Center for Fusion Energy Science and Technology, Chinese Academy of Engineering Physics, Beijing 100088, China.

[4] Brookhaven National Laboratory, Upton, New York 11973, USA

[5] Hefei National Laboratory for Physical Sciences at the Microscale, University of Science and Technology of China, Hefei, Anhui 230026, P. R. China

[6] Key Laboratory of Strongly-Coupled Quantum Matter Physics, Chinese Academy of Sciences, Hefei, Anhui, 230026, P. R. China

[7] Collaborative Innovation Center of Advanced Microstructures, Nanjing, Jiangsu, 210093, P. R. China

Abstract:

The widely spread oxygen vacancies (V$_O$) in multiferroic materials could strongly affect their physical properties. However, their exact influence has rarely been identified in hexagonal manganites. Here, with the combined use of transmission electron microscopy (TEM) and first-principles calculations, we have systematically studied the electronic and crystal structure modifications induced by V$_O$ located at the same Mn atomic plane (in-plane V$_O$). Our TEM experiments reveal that the easily formed in-plane Vo not only influence the electronic structure of YMnO$_3$ but alter the

in-plane Wyckoff positions of Mn ions, which may subsequently affect the intra-plane and inter-plane exchange interaction of Mn ions. The ferroelectricity is also impaired due to the introduction of V_O. Further calculations confirm these electronic and structural changes and modifications. Our results indicate that the electronic and crystal structure of $YMnO_3$ can be manipulated by the creation of V_O.

Ⅰ. INTRODUCTION

$YMnO_3$, a fascinating first class single phase multiferroic material [1,2], has aroused worldwide attention in the past decade. Its ferroelectric properties are determined by A sites Y ions, while its (anti)ferromagnetic properties by the B sites Mn ions [3]. The hexagonal structure (space group $P6_3cm$) controls its uniaxial anisotropy of ferroelectricity. In $YMnO_3$, the ferroelectricity emerges in two steps. At 1270K, tilting of the MnO_5 bipyramids and corrugation of Y ions occur. At 920K, the displacements of Y ions cannot be counteracted, thus the net ferroelectricity develops [4]. During this process, the trimerization of nearby three MnO_5 bipyramids plays an important role. The three MnO_5 clusters tilt together (as shown in Fig. 1) to induce the ferroelectric displacements of Y ions and thus the $YMnO_3$ is also called improper ferroelectric material [5]. In the trimerization process, only MnO_5 bipyramids tilt together and Mn still stay at 1/3 high symmetric position [3,6]. Moreover, due to the close relationship between positions of Mn ions and (anti)ferromagnetism, $YMnO_3$ is a representative magnetoelastic material [6]. The positions of Mn ions not only affect the intra-plane exchange interactions but also tune the signs of inter-plane

super-superexchange interactions [7]. A specific magnetic configuration is determined by the positions of Mn ions in order to release spin frustration. Fabrèges, *et al* have conducted experiments to testify the strong magnetoelastic coupling, finding that the key parameter determining the sign of the interlayer exchange coupling is whether the position of Mn ion is larger or smaller than 1/3 [7]. However, neither experiments nor theoretical calculations provide matchable results on the positions of Mn ions [8]. The Wyckoff coordinate x can be either more than or less than 1/3, while this value is exactly 1/3 in the density-functional theory (DFT) results [9]. Gibbs, *et al* supposed that Mn has the smallest neutron scattering length and its position is the least well-determined parameter [10]. Prikockytė , *et al* proposed that their DFT calculations do not predict positions of Mn ions well [9], because first-principles calculations are conducted at 0 K and non-collinear magnetic moment should be considered to achieve a better description of the positions of Mn ions. We have also conducted a series of first-principles calculations and found that whatever the initial configurations are, Mn ions will finally relax back to positions at 1/3. Though different results have been obtained for the positions of Mn ions, a consensus has been reached that only in-plane shifts can occur for Mn ions. To sum up, though position of Mn ion is a crucial parameter for the electronic structure, the theoretical results and experimental results are not in agreement with each other. Therefore, the underlying mechanism leading to various Wyckoff coordinates of Mn ions deserves exploration.

This contradiction might result from the existence of local defects. As one of the

widely-existing defects, oxygen vacancies (V_O) can greatly influence materials in various aspects, such as the introduction of interface dead layers [11], variation of the diffraction intensity due to the subtle change of local structures [8], and the pinning of the vortex cores of topological domains [12]. We thereby conduct a series of experiments by transmission electron microscopy (TEM), discovering that formation of in-plane V_O is likely to yield the in-plane deviations of Mn ions from 1/3 position. Through first-principles calculations, we further confirm the structural change affected by the in-plane V_O. In the light of our results, we demonstrate the positions of Mn ions can be influenced by the in-plane V_O, which may finally lead to the magnetic properties variation within the local area.

II.EXPERIMENTAL DETAILS

Figure 1(a) is a typical hexagonal crystal unit cell of $YMnO_3$ with downward polarization. The nearby three MnO_5 clusters in each Mn-O plane tilt together to induce non-centrosymmetric movements of Y ions. The oxygen atoms in MnO_5 clusters can be roughly classified into two types：the in-plane oxygen atoms (O_P) which locate at the same plane with Mn ions, and the on-top oxygen atoms (O_T) which locate at the apexes of MnO_5 clusters. The Wyckoff position O_P is composed of O_{P1} and O_{P2}, while O_T is consist of O_{T1} and O_{T2} as shown in Fig.1.
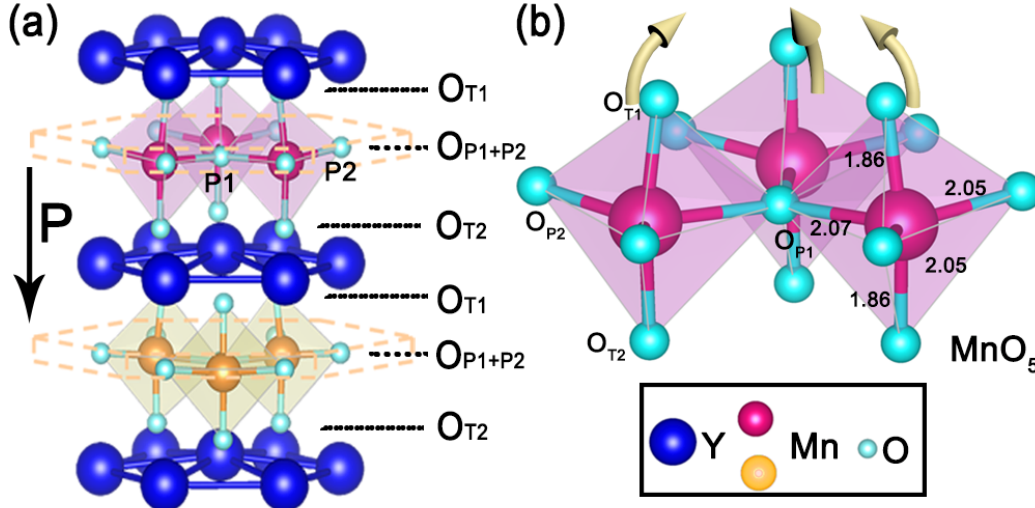
FIG. 1. (Color online) The ideal atomic model of YMnO₃. (a) The hexagonal crystal unit cell of $YMnO_3$ with downward polarization direction. The atoms surrounded by yellow dashed line represent the positions of O_P atoms, which is the main part we are going to discuss. The atomic planes of O_T are also indicated. (b) The nearby three MnO_5 clusters extracted from (a). The bond lengths in a typical MnO_5 cluster are also demonstrated in angstrom unit [9]. The yellow arrows represent the directions that the three MnO_5 clusters tilt.

We take advantage of electron energy loss spectroscopy (EELS) to study the electronic structures of $YMnO_3$. EELS is a widely used method to detect the discrete transitions between atomic energy levels, and allows composition and hybridization information analysis [13,14]. Particularly, the near-edge fine structure contains hybridization information about the nearest-neighbored bonding (O_{2p}-orbital and $3d$-orbital of transition metal). Our EELS spectra are acquired by the 300kV FEI Titan 80-300 spherical aberration corrected (Cs-corrected) TEM, equipped with a Gatan

Tridium EELS system. In order to improve the signal/noise ratio of the EELS spectra, the Cs-corrected TEM was operated in the diffraction mode. The blue line in Fig. 2(a) shows the O K-edge of the EELS spectrum acquired from the single crystalline $YMnO_3$ TEM sample, from which four peaks (a-d) can be identified. The four peaks are positioned at 531.2, 533.8, 538.1 and 542.5 eV, respectively, calibrated by the corresponding zero-loss-peak of each spectrum. We have also calcined a $YMnO_3$ sample in argon atmosphere at 1000℃. The sample shows an apparent phase separation phenomenon: one region contains only Mn/O elements while the other contains only Y/O elements. The EELS spectra acquired from these two regions are shown as red and black lines in Fig. 2(a). Comparing our results with the published one [15], we can find that Mn^{2+} and Mn^{3+} coexist in Mn-O region. In the red dotted line, Peak a and Peak d represent the existence of Mn_2O_3, while Peak b and Peak d demonstrate the presence of MnO. Since Mn ions in $YMnO_3$ mainly show +3 valence state, here we only focus on the positions of Peak a and Peak d at Mn-O region. From the black line in Fig. 2(a), we know that only a little oxygen deficiency exists in Y-O region [16]. For Y_2O_3, the absence of the prepeak of the O K-edge around 532 eV indicates that it is an insulator with completely filled O_{2p} states [17]. From the EELS spectra of $YMnO_3$, Mn-O and Y-O regions (as shown in Fig. 2(a)), we conclude that, in $YMnO_3$, Peak b and Peak c represent the hybridization between Y and O while Peak a and Peak d represent the hybridization between Mn and O. Moreover, for $YMnO_3$ and Mn_2O_3, there is a prepeak around 532 eV which is very close to the bonding energy of oxygen. The prepeak around 532 eV (Peak a) can be attributed to

the electron transitions from O_{1s} to the unoccupied O_{2p} state and its appearance in YMnO$_3$ is a reflection of the presence of holes on oxygen sites, which leads to p-type conductivity [17].

During the experiment, we also observed the evolution of the oxygen pre-K-edge (normalized by Peak b) in YMnO$_3$ under electron beam irradiation, as shown in Fig. 2(b). It should be noticed that Peak a and Peak d gradually disappear within tens of seconds and Peak c shrinks a little at the same time. In TEM, the sample is under high vacuum condition where V_O can easily form and the electron beam irradiation can promote the loss of oxygen [18]. Such phenomena were particularly observed when the EELS acquisition is done in diffraction mode where high electron dose per area was used. In contrast, if we only use image mode (the same condition for high resolution TEM imaging), little change of the oxygen pre-edge peak intensity was observed. In this experiment, we first take HRTEM images at an area with nearly stoichiometric oxygen, then use high electron dose (the diffraction mode) to create V_O. When the contents of V_O become stable, we take another HRTEM image and compare these two images.

The gradual decrease of Peak a and Peak d indicates the gradual decrease of hybridization between Mn and O. In contrast to the sharp decrease of Peak d and Peak a, Peak c representing the Y-O hybridization only has slightly changes, thus the Y-O bonds can hardly be influenced by the electron beam irradiation induced oxygen deficiency, but the Mn-O bonds are strongly affected. Furthermore, it can be inferred that the loss of O_P is more than that of O_T as we discuss the facts below. The bond

number ratio of Mn-O_P and Mn-O_T is 3:2 in MnO_5 cluster and that of Y-O_P and Y-O_T is 1:3 in YO_8 cluster. Since O_P take up most of Mn-O hybridization and only a small part of Y-O hybridization (from the bond number ratio), the disappearance of O_P will have a larger influence on Mn-O hybridization than on Y-O hybridization. In Fig. 2(b), the relative height changes of Peak b and Peak c can be explained by the formation of O_P vacancies, which have small influence on Y-O_P hybridization. Therefore, we can conclude that O_P is more unstable than O_T. Our DFT calculations also support this point of view as shown in the latter sections. According to the thermodynamic calculation, the free energies needed to deoxidize Y_2O_3, Mn_3O_4 and PbO are 1623, 423 and 124 kJ/mol, respectively [19]. Hence, the oxidizing ability of Y is much larger than that of Mn, which is in consistence with our experimental results. The X-ray absorption spectroscopy (XAS) is also a commonly used method to study the hybridization phenomenon in materials. Comparing our EELS results in Fig. 2(a) with XAS data published previously [20, 21], we found that the position of Peak a positioned at the Mn_{3d}-O_{2p} hybridization zone , while Peak b and Peak c correspond to the Y_{4d}-O_{2p} hybridization zone in XAS spectra, indicating that our results are compatible with XAS.

Figure 2(c) shows the dynamic behaviors of Mn $L_{2,3}$-edge acquired at the same time with O K-edge, from which we could get the valence states of Mn ions. As what we have already known, the more Vo, the less valence states of Mn ions. We can calculate the Mn oxidized states by quantifying the L_3/L_2 area ratios and also the Mn/O ratios at the same time. The initial state of Mn ions is about +3 and Mn:O ratio

is 1:3. With the electron beam irradiation, the valence states of Mn ions drop via +2.8, +2.6 down to +2.5. Further electron beam irradiation did not increase oxygen deficiency. The Mn/O ratio becomes stable (to be 1:2.75) when irradiation time exceeds 18s, whose underlying mechanism is unknown at this point. Possible scenario can be due to the chemical drive force that leads to nearby oxygen diffuse to the oxygen deficiency area to compensate the loss of oxygen induced by electron beam irradiation, or the requirement of higher energy of electron beam to further create V_O.
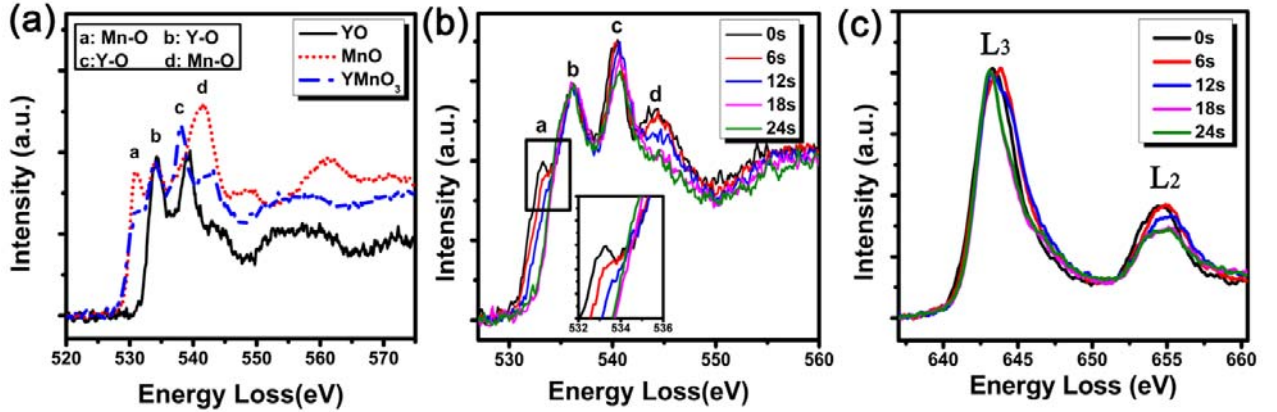

FIG. 2. (Color online) EELS spectra of $YMnO_3$. (a) Combination of EELS spectra from $YMnO_3$ single crystalline, Mn-O and Y-O regions. (b) Variation of O-K edges of $YMnO_3$ within tens of seconds of electron beam irradiation. Peak a and Peak d tend to disappear in a short time. (c) Variation of Mn-$L_{2,3}$ edges acquired along with (b).

In order to understand V_O induced structural changes, we have acquired HRTEM images before and after the creation of V_O. Figures 3(a) and 3(d) are captured by the Cs-corrected TEM with negative spherical aberration correction technique (NCSI) [22]. The NCSI technique allows not only the determination of atomic species, but

also the measurement of atomic positions with a precision of a few picometers [23]. The atom-columns show bright contrast on dark background under the best defocus condition. Figures 3(a) and 3(d) are taken at [110] zone axis – the only zone axis that can observe the ferroelectric displacement of Y ions. Atoms in a straight line without shifting up and down are Mn ions. Atoms with up-up-down configurations are Y ions which have upward polarization direction. The corresponding atomic model from [110] zone axis is superimposed at the top-right corner of Fig. 3(a). We have simulated HRTEM images using MacTempasX commercial software based on the multi-slice method [24], and the simulated result is shown in the white rectangle in Fig. 3(a). The defocus value and the thickness of the sample are estimated to be 6 nm and 3 nm, respectively. Possibly due to the small distance with nearby atoms, the oxygen atoms are not very clear in the HRTEM images, which is in accordance with our simulated HRTEM image. Atomic positions were found by the least-squares fit using the two-dimensional Gaussian profiles. Figure 3(a) shows the initial atomic arrangement before the electron beam irradiation. After getting this image, we change TEM to diffraction mode and use electron beam to create V_O for about 30 seconds. Then we get another HRTEM image showing in Fig. 3(d). We have located the positions of Mn ions in each unit cell and calculated their relative positions with respect to the 1/3 Wyckoff position. We note that   the displacement of Mn ions varies from several picometers up to twenty picometers in different unit cells. Figures. 3(b) and 3(e) show the contour maps of the mapping results from Figs. 3(a) and 3(d) respectively, from which we can find that Mn ions locate close to 1/3 Wyckoff

position in Fig. 3(a), while deviate largely from 1/3 position for most unit cells in Fig. 3(d), *i.e.* the color in Fig. 3(b) is more uniform than that in Fig. 3(e). The average results stemming from neutron diffraction experiments cannot reflect the actual Mn positions in each unit cell. The EELS spectra corresponding to Figs. 3(a) and 3(d) are shown in Figs. 3(c) and 3(f), respectively, demonstrating that Fig. 3(d) has more V_O than Fig. 3(a) due to the disappearance of Peak a and Peak d in EELS spectrum. As we discussed earlier, these V_O located at in-plane positions will lead to the large in-plane movements of Mn ions in Fig. 3(e).
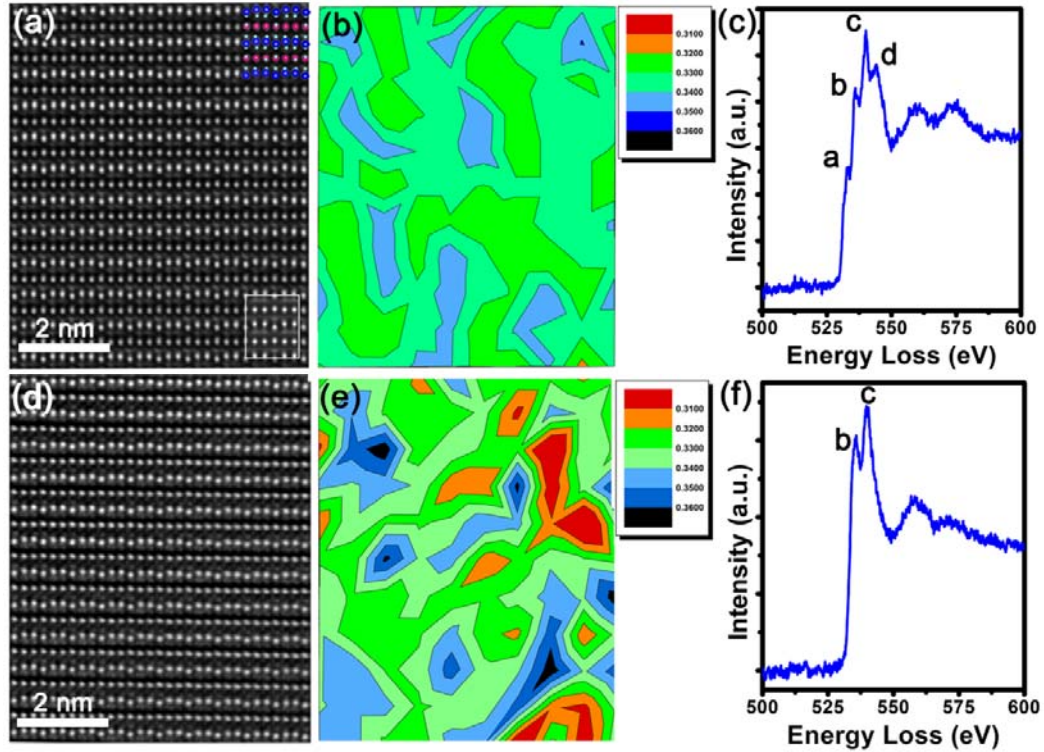

FIG. 3. (Color online) HRTEM images of YMnO$_3$ single crystalline at [110] zone axis and the corresponding Mn positions mappings. (a) HRTEM image of nearly stoichiometric area. Atoms shifting up and down are Y and atoms in a line are Mn. The atomic model of YMnO$_3$ is superimposed on the image where blue atoms

11

represent Y and red atoms represent Mn. The inset in the white rectangle locates at the bottom-right corner shows the simulated HRTEM image. (b) Mn positions mapping in contour map format calculated from (a). Different colors mean different positions of Mn ions relative to 1/3 position in each $YMnO_3$ unit cell. (c) EELS spectrum acquired along with (a). (d) HRTEM image of oxygen deficient area. (e) Mn positions mapping calculated from (d). (f) EELS result acquired along with (d).The disappearance of Peak a and Peak d represents the missing of oxygen atoms as we discussed above.

To correlate the V_O to local atomic displacement observed in Figs. 3(a) and 3(d), we calculate the local ferroelectric polarization using the following equation [25]:

$$P_s = (\sum Z_i^* \delta_i)/V = (3.6e/V) * \sum \frac{\delta}{2} = 0.15 * \delta(\frac{\mu C}{cm^2 * pm}) \quad (1)$$

where P_s is ferroelectric polarization value of a unit cell; Z_i^* is Born effective charges of Y ions, which is $3.6e$ according to DFT calculation results [3]; δ_i is the atomic displacement of Y ions relative to their positions in paraelectric phase, which is about the half value of δ, as shown in Fig. 4(a) [26], V is the volume of a unit cell. We locate the positions of Y ions with Gaussian profiles in HRTEM images and calculated the δ value per unit cell using the atomic positions of Y ions. In Figs. 3(a) and 3(d), each row has 10 $YMnO_3$ unit cells and the row average ferroelectric polarization values are shown in Fig. 4(b). We can easily notice that the ferroelectric polarization values in oxygen deficiency area are smaller than that of nearly stoichiometric area. In nearly stoichiometric area (Fig. 3(a)), the ferroelectric polarization value is about 6 $\mu C/cm^3$ which is very close to the bulk value of $YMnO_3$

[3]. However, in oxygen deficiency areas, the ferroelectric values reduce to about 2/3 of bulk value.
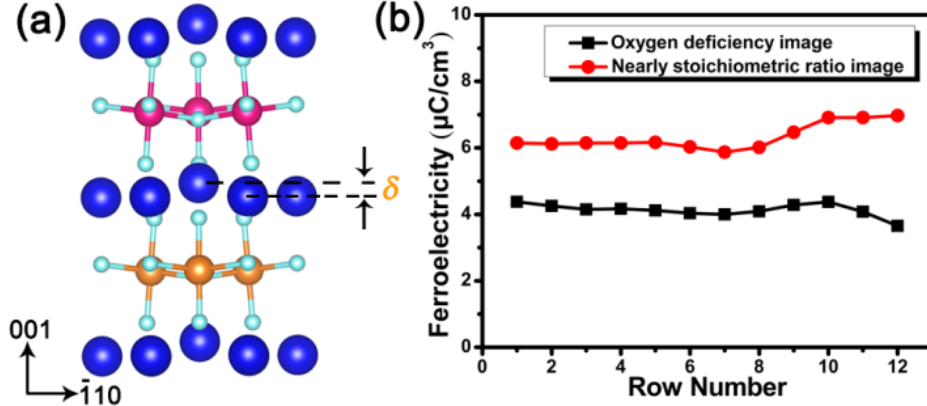

FIG. 4. (Color online) Calculations of ferroelectric polarization values from HRTEM images. (a) YMnO₃ hexagonal crystal model from [110] zone axis where we could observe the ferroelectric displacement. δ value is defined. (b) Calculated ferroelectric values from HRTEM images in Fig. 3(a) and 3(d). The introduction of V_O can reduce the ferroelectric displacements.

In Fig 3(d), though the ferroelectric values are smaller, we can still observe ferroelectric displacement. In typical single crystal YMnO₃, Mn ions locate at the centers of MnO₅ bipyramids instead of the centers of MnO₆ octahedrons, thus YMnO₃ is not a Jahn-Teller active material. Mn $3d$ orbital is split into two doublets: e_{1g} (zx/yz) and e_{2g} (xy/x^2-y^2), and one singlet: a_{1g} (z^2) [27]. The lowest d band (e_{1g}) is quite localized, while the middle band (e_{2g}) shows more dispersion. The highest band (a_{1g}) is localized again, which is contrary to the usual situation [28]. In this structure, since the O-O distance along z direction is long, the weak O-O interaction in the z direction

limits the bandwidth. Thus the whole conductivity of the material is determined by the e_{2g} states. Oxygen vacancies induced electron doping will occupy the z^2 states, which hardly influence the conductivity of $YMnO_3$. Even though the formation of oxygen vacancies, the conductivity of $YMnO_3$ is still low and the ferroelectricity still remains. Forming oxygen vacancies in $YMnO_3$ will result in a mixed valence state of Mn^{2+}-Mn^{3+}, which yields a high spin state for the Mn ions.

In order to confirm the in-plane off-centered movements of Mn ions caused by V_O, we also take HRTEM images from [001] zone axis. The $YMnO_3$ shows six-fold symmetry in this zone axis and the typical atomic model is presented in the inset of Fig 5(c). Figure 5(a) shows the initial positions of Mn ions at nearly stoichiometric area. After 30 seconds electron beam irradiation, we take another HRTEM image as shown in Fig. 5(c), and then compare the positions of Mn ions. We compare experiment and simulation as shown in the inset of Fig. 5(a). The defocus value and the thickness of this area are estimated to be 3nm and 2nm. As we stated above, the position change of Mn ions is clearly influenced by thein-plane V_O.
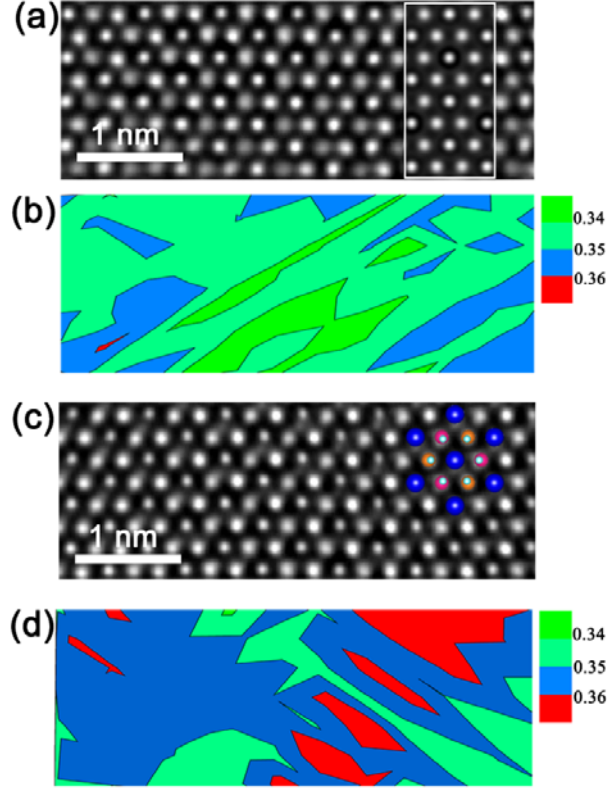
FIG. 5. (Color online) HRTEM images of YMnO$_3$ single crystalline at [001] zone axis and the corresponding Mn positions mappings. (a) HRTEM image with nearly stoichiometric ratio which is taken before electron beam irradiation. The positions of Mn ions can be recognized with the help of YMnO$_3$ atomic model in (c). The inset in the white rectangle locates at the right side shows the simulated HRTEM image. The defocus value is 3nm and the thickness of the sample is 2nm. (b) Mn positions mapping in contour map format calculated from (a). Different colors mean different positions of Mn ions relative to 1/3 position for every Mn ions' column. (c) HRTEM image which is taken after electron beam irradiation. The inset is the YMnO$_3$ atomic model shows the configuration at [001] zone axis. (d) Mn positions mapping calculated from (c).

Ⅲ.DETAILS OF CALCULATIONS

In order to confirm above conclusions theoretically, the formation energies of different V_O sites are calculated through first-principles methods. We perform first-principles-based DFT calculations within the local spin-density approximation plus Hubbard U (LSDA+U) [29] as implemented in the *Vienna ab initio Simulation Package* (VASP) [30]. Projector-augmented wave method is used with a cutoff energy of 500 eV (the accuracy has been checked to be sufficient) [31]. We employ the values of on-site Coulomb interaction U=8eV and exchange parameter *J*=0.88 eV for the Mn *d*-orbital [32]. We relax the atomic positions using the conjugate gradient algorithm until the residual forces are smaller than 0.01 eV/Å [33]. A 4×2×2 Gamma k-mesh is used for relaxation and a 4×4×4 k-mesh is used for the formation energy calculations.

The formation energies are calculated from $E_{form} = E_{vacancy} + \mu - E_{perfect}$, where μ is the chemical potential of removed atoms, $E_{vacancy}$ and $E_{perfect}$ are the total energy with and without the concerned vacancy. In the case of V_O, we consider the growth conditions of different partial pressures of oxygen and the formation energy be a variable that is linearly dependent on the oxygen chemical potential. We define the O-rich condition by taking the O chemical potential half the chemical potential of an O_2 molecule and define the O-poor condition by using μ(O)= (μ(YMnO₃)- μ(Y)-μ(Mn))/3, where μ(Y) and μ(Mn) are the potentials of Y ion and Mn ion respectively.

In our calculations, removal of one oxygen atom from a 30-atom cell corresponds to a vacancy concentration of 5.6%. Figure 6 shows the formation energy from the O-poor (left) to the O-rich (right) conditions. The figure indicates that V_O can indeed spontaneously form in the O-poor condition since $E_{form}<0$ and O_P vacancies are much easier to form than O_T vacancies. The formation energy of O_{P2} vacancies is the smallest, representing O_{P2} vacancies being the easiest to form among all sites of oxygens. The formation energy of O_{P1} vacancies is 1.49meV higher than that of O_{P2} vacancies and the formation energy of O_{T2} vacancies is 9.34meV higher than that of O_{T1} (see the insets of Fig. 6), whose values are much smaller than the energy gap between O_T and O_P vacancies. Thus, we could conclude that O_{P1} and O_{P2} nearly have equal probability to loss, and so do the oxygen atoms in different axial positions.
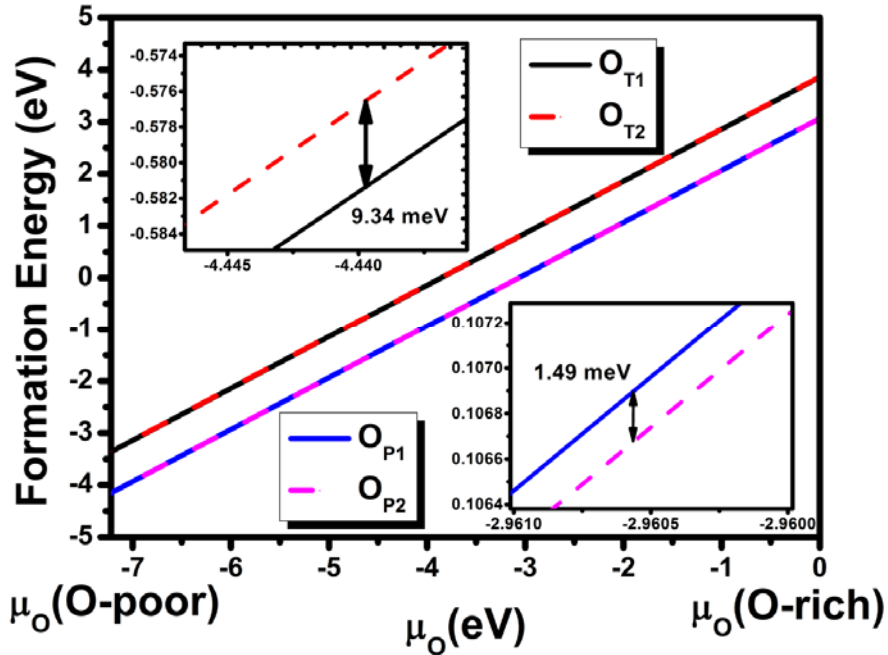

FIG. 6. (Color online) DFT calculated formation energy of V_O at different sites as a function of the chemical potential of oxygen. The insets show the magnified

differences of V_O formation energy.

In our DFT calculations, $YMnO_3$ unit cell with four typical sites of V_O (vacancies at O_{T1}, O_{T2}, O_{P1}, and O_{P2}) are built and relaxed, and the relaxed crystal structures are depicted in Figures 7(a)-7(e). In the perfect stoichiometric $YMnO_3$, Mn ions relax to the positions of $x=1/3$ [9] and Mn ions locate at the high symmetry positions and under symmetric ligand fields (MnO_5, D_{3h} site symmetry). As shown in Table Ⅰ, the configurations with different V_O sites result in the deviations of Mn ions from 1/3 position, and O_P vacancies may lead to the in-plane movements of Mn ions by several picometers to nearly twenty picometers, which agree well with our experiments. Figures 7(a) and 7(b) show that O_{P1} vacancies push the Mn ions to theWyckoff positions larger than 1/3, while O_{P2} vacancies move Mn ions to the Wyckoff positions smaller than 1/3. In contrast, O_T vacancies give rise to less significant changes of the in-plane Mn position than O_P vacancies.
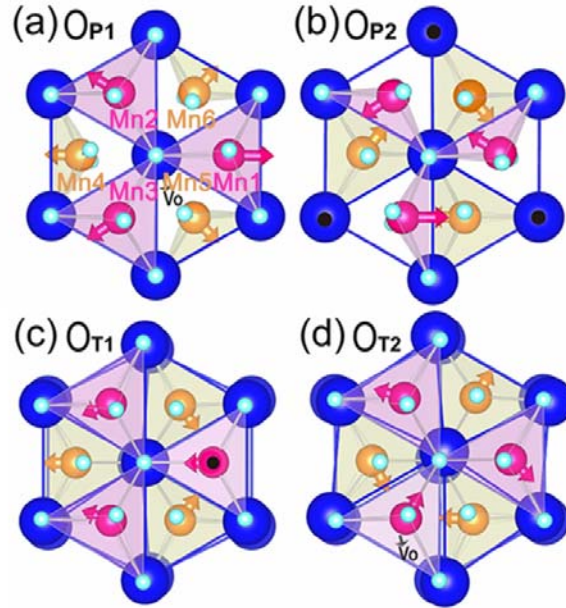

FIG. 7. (Color online) (a)-(d) Relaxed structures by DFT calculations with different

sites of V_O in which the red and yellow arrows on the sites of Mn ions represent the directions and quantities of the movements of Mn ions from 1/3 position. Sites of V_O are represented by black dots in (b) and (c), while marked with short black arrows in (a) and (d) because they are invisible in [001] zone axis. Positions of six Mn ions in the hexagonal unit cell of $YMnO_3$ are indicated in (a).

TABLE Ⅰ : In-plane movements of Mn ions away from the 1/3 position in different configurations of V_O.

	In-plane movements of Mn ions(pm)					
	Mn1	**Mn2**	**Mn3**	**Mn4**	**Mn5**	**Mn6**
O_{P1}	18.0	11.1	12.2	9.4	8.8	9.0
O_{P2}	11.6	11.7	18.1	9.4	8.9	9.0
O_{T1}	0.8	1.9	1.8	5.8	4.4	4.4
O_{T2}	3.5	3.5	1.8	6.9	6.9	3.4

Figure 8 shows the calculated electronic density of states (DOS) for the perfect $YMnO_3$ and oxygen-deficient $YMnO_3$. Since O_P vacancies have similar DOS and nearly degenerate energies, only the DOS of O_{P2} vacancy is analyzed for simplicity. For the same reason, the DOS of O_{T1} vacancy is shown as the representative of O_T vacancies. From Fig. 8 (a), the valence bands are mainly composed of O electrons and Mn electrons take up most of the conduction bands. This feature is general in perovskite ferroelectrics in which the conduction bands are contributed by d states of

transitional metal and O *p* states contribute to the valence bands. When the oxygen

vacancies are introduced, in-gap states emerge as the defects states occupied by Mn

electrons. Since an oxygen vacancy can bring two extra electrons, these electrons

naturally fill in the nearby Mn orbitals. As shown in Figs. 8 (b) and 8(c), the defect

states in $YMnO_3$ with O_T vacancies have higher energies than those in $YMnO_3$ with

O_P vacancies. That is why the O_P vacancies are more energy-saving than the O_T

vacancies. Note that the Fermi energy is crossed by Mn states in systems with O_T

vacancy, in principle it is impossible to maintain ferroelectricity since the system is

conductive. However, in experiments ferroelectricity will not be totally diminished

since the vacancy-induced charge carriers tend to localize around the vacancy and
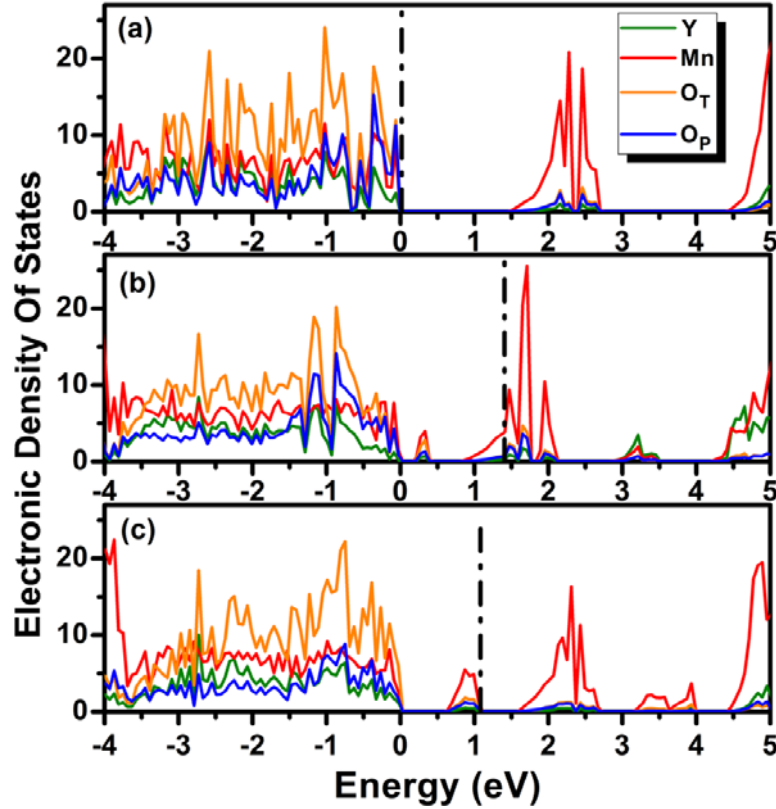
cannot screen all the polarization.

FIG. 8. (Color online) Calculated electronic density of states for (a) perfect $YMnO_3$, (b) $YMnO_3$ with O_{T1} vacancy and (c) $YMnO_3$ with O_{P2} vacancy. The valence bands maximum is set to zero and the Fermi energies are denoted by the dashed lines.

We further conduct simulations to support our experimental EELS spectra [34]. FEFF 9 code can be employed to calculate the EELS spectra of O K-edge [35]. The O K-edge EELS spectra for four unequivalent positions of O atoms (O_{P1}, O_{P2}, O_{T1}, O_{T2}) are calculated and exhibited in Figs. 9(b) and 9(e). The weighted average of atomic fraction of the four spectra is shown in Fig. 9(a), which is used to compare with our experimental observations. Considering the actual experimental energy resolution, a convolution with a Gauss function with 1eV standard deviation is applied to each spectrum [36]. The four main peaks shown in Fig. 9(a) are consistent with our experimental results in Fig. 2(a). Comparing Fig. 9(a) with other four Figs. 9(b)-9(e), we find that in-plane oxygen atoms contribute to the peak *a*, *b* and *d* , on-top oxygen atoms mainly contribute to the peak *b*, *c* and *d* in the spectra. Because every in-plane oxygen atom has three nearest neighbor Mn ions and a Y ion, and every on-top oxygen atom has three nearest neighbor Y ions and a Mn ion, the main contribution to EELS for in-plane oxygen atom is from MnO and that of top-plane oxygen atom is from YO. This is consistent with experimental results shown in Fig. 2(a).
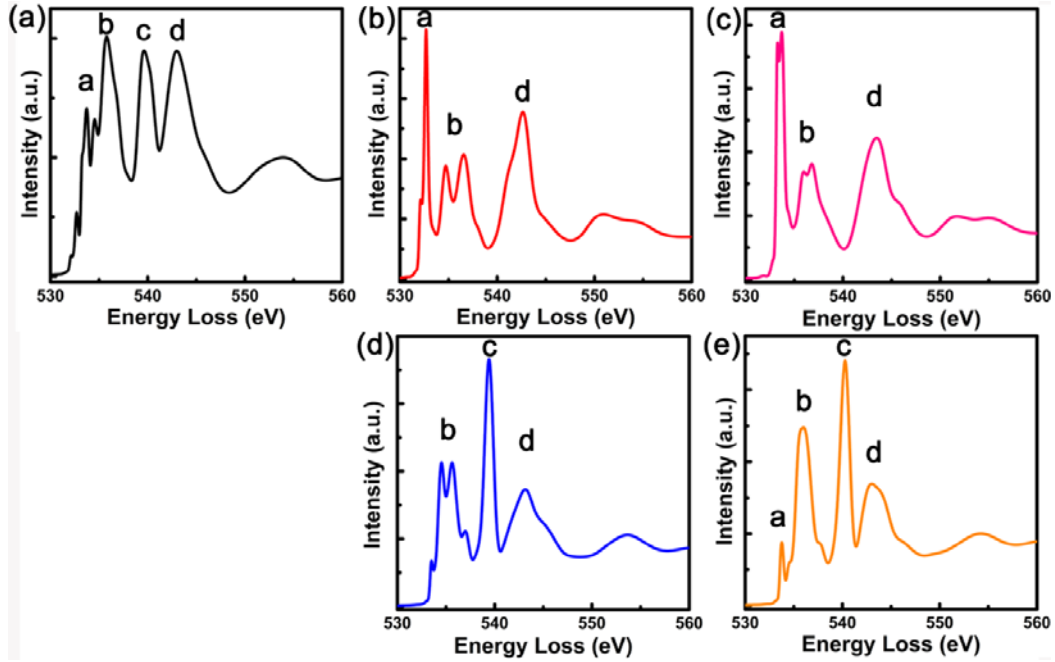
21

FIG. 9. (Color online) The calculated O K-edge EELS spectra. The EELS spectra for four unequivalent positions O_{P1} (b), O_{P2} (c), O_{T1} (d) and O_{T2} (e) are calculated, and (a) is the weighted average of atomic fraction of the four spectra from (b) to (e).

The total EELS spectra for $YMnO_3$ unit cells with four kinds of oxygen vacancies are also calculated with FEFF code. Using VASP, we first obtain relaxed structures with oxygen vacancies as shown in Fig. 7, then use the relaxed structures to calculate the EELS spectra. The EELS spectra of all unequivalent oxygen atoms near oxygen vacancy are calculated, and the final spectra are the average of these EELS spectra based on their atomic occupancy. Figure 10 shows the calculated results. From our calculation results, we find that the peak *a* of the EELS spectra disappears when oxygen vacancy are at O_{P1} and O_{P2} positions and the intensity of Peak *d* also decreases. On the contrary, Peak a remains and the intensity of peak d does not drop when oxygen vacancies are at O_{T1} and O_{T2} positions, which agrees with experimental
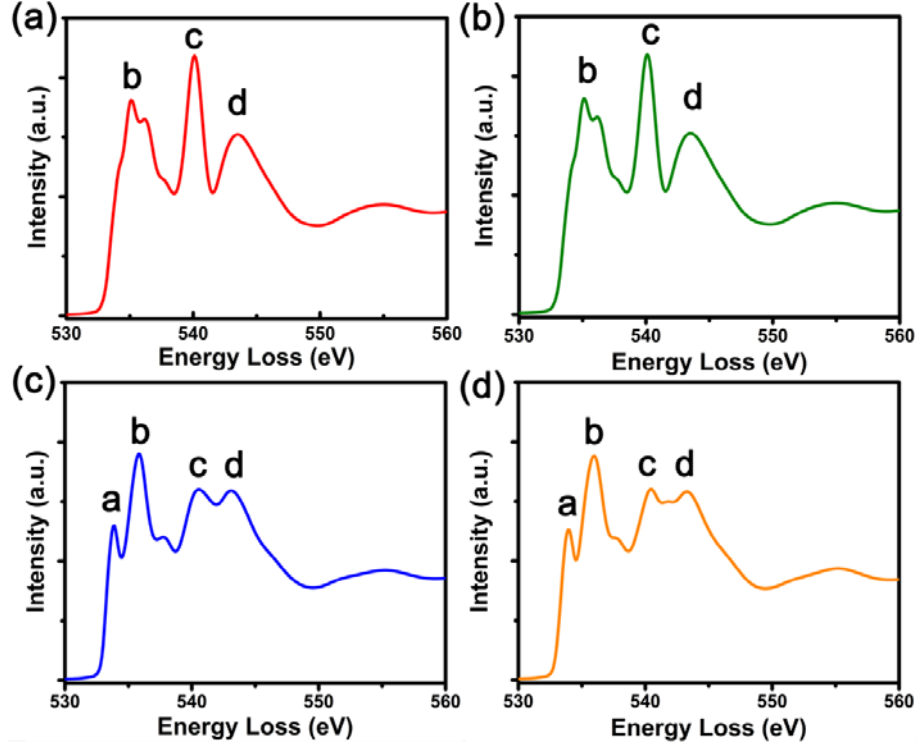
measurements.

FIG. 10. (Color online) The calculated total EELS spectra for $YMnO_3$ unit cell with different sites of V_O. EELS spectrum for DFT relaxed $YMnO_3$ unit cell with O_{P1} vacancy (a), O_{P2} vacancy (b), O_{T1} vacancy (c) and O_{T2} vacancy (d).

Ⅳ. CONCLUSIONS

In summary, we have conducted a series of experiments and calculations to show that oxygen vacancies can strongly influence the electronic and crystal structures of $YMnO_3$. From EELS spectra analyses, we identify the meaning of four peaks in O K-edge for $YMnO_3$. Besides, we can deduce that O_P vacancies are more likely to form than O_T vacancies and O_P vacancies can impair the hybridization of Mn-O, which has been confirmed by further calculations. The average position of Mn ions derived from

neutron diffraction experiments does not reflect the real positions of Mn ions when oxygen vacancies are present. With the help of the state-of-the-art spherical-aberration-corrected HRTEM, we are able to verify the positions of Mn ions in each unit cell for different oxygen contents and the result are confirmed by our DFT calculations. Their corresponding ferroelectric polarization is also determined. We note only in the ideal stoichiometry samples, do Mn ions occupy the 1/3 position, as predicted by DFT. Our finding fills the gap between theoretical calculation and experimental results on the positions of Mn ions, and shed light on how the oxygen vacancies induced local anomalous in multiferroic properties.

V.ACKNOWLEDGMENT

References:

[1]S. Picozzi, and C. Ederer, J. Phys.: Condens. Matter **21**, 303201 (2009)

[2]D. Khomskii, Physics **2**, 20 (2009)

[3] B. Van Aken, T. Palstra, A. Filippetti, N. Spaldin, Nat. Mater. **3**, 164, (2004)

[4]T. Jungk, A. Hoffmann, M. Fiebig, and E. Soergel, Appl. Phys. Lett **97**, 012904 (2010)

[5]C. J. Fennie and K. M. Rabe, Phys. Rev. B **72**, 100103 (2005)

[6] L. Seongsu, A. Pirogov, M. Kang, K. –H. Jang, M. Yonemura, T. Kamiyama, S.-W. Cheong, F. Gozzo, N. Shin, H. Kimura, Y. Noda, and J. –G. Park, Nature, **451**, 805(2008).

[7]Fabrèges X., Petit S., Mirebeau I., Pailhès S., Pinsard L., Forget A., Fernandez-Diaz M., Porcher F., Phys. Rev. Lett. **103**, 067204 (2009)

[8]S. Cheng, S. Q. Deng, Y. G. Zhao, X. F. Sun, and J. Zhu, Appl. Phys. Lett. **106**, 062905 (2015)

[9] Prikockytė A. , Bilc D., Hermet P., Dubourdieu C., and Ghosez P., Phys. Rev. B **84**, 214301 (2011).

[10]A. S. Gibbs, K. S. Knight, and P. Lightfoot, Phys. Rev. B **83**, 094111 (2011).

[11] L. Zhipeng *et al.*, Adv. Funct. Mater. **22**,4312 (2012).

[12]M.-G. Han, Y. Zhu, L. Wu, T. Aoki, V. Volkov, X. Wang, S. Chae, Y. Oh, and S.-W. Cheong, Adv. Mater. **25**, 2415 (2013).

[13]J. Taftø and J. Zhu, Ultramicroscopy 9, 349 (1982).

[14]R. F. Egerton, *Electron Energy-Loss Spectroscopy in the Electron Microscope* (Springer Science + Business Media, New York, 1996).

[15]H. K. Schmid and W. Mader, Micron **37**, 426 (2006).

[16]A. Travlos, N. Boukos, G. Apostolopoulos, and A. Dimoulas, Appl. Phys. Lett. **82**, 4053 (2003).

[17]H. L. Ju, H.-C. Sohn, and K. M. Krishnan, Phys. Rev. Lett. **79**, 3230 (1997).

[18]R. F. Egerton, P. Li, M. Malac, Micron **35**, 399 (2004)

[19]N. Fujimura, S. Azuma, N. Aoki, T. Yoshimura, and T. Ito, J. Appl. Phys. **80,** 7084 (1996).

[20]D. Y. Cho, S. –J. Oh, D. G. Kim, A. Tanaka, and J. –H. Park, Phys. Rev. B **79**, 035116 (2009)

[21]S. H. Liu, J. H. A. Huang, X. Qi, W. J. Lin, Y. J. Siao, C. R. Lin, J. M. Chen, M. T. Tang, Y. H. Lee, and J. C. Lee, AIP Advances **1**, 0321730-1(2011)

[22]K.W. Urban, Science, **321**, 506 (2008)

[23]C. L. Jia, K. W. Urban, M. Alexe, D. Hesse, and I. Vrejoiu, Science, **331**, 1420 (2011)

[24]Y. Yu, X. Zhang, Y. G. Zhao, N. Jiang, R. Yu, J. W. Wang, C. Fan, X. F. Sun, and J. Zhu, Appl. Phys. Lett. **103**, 032901 (2013)

[25]D. D. Fong, C. Cionca, Y. Yacoby, G. B. Stephenson, J. A. Eastman, P. H. Fuoss, S. K. Streiffer, Carol Thompson, R. Clarke, R. Pindak, and E. A. Stern, Phys. Rev. B **71**, 144112 (2005)

[26]A. S. Gibbs, K. S. Knight, and P. Lightfoot, Phys. Rev. B, **83**, 094111, (2011).

[27]D. –Y. Cho, J. –Y. Kim, B. –G. Park, K. –J. Rho, J. –H. Park, H. –J. Noh, B. J. Kim, S. –J. Oh, H. –M. Park, J. –S. Ahn, H. Ishibashi, S –W. Cheong, J. H. Lee, P. Murugavel, T. W. Noh, A. Tanaka, and T. Jo, Phys. Rev. Lett. **98**, 217601 (2007)

[28]Bas B. Van Aken, Jan-Willem G. Bos, Robert A. de Groot, and Thomas T. M. Palstra, Phys. Rev. B **63**, 125127 (2001)

[29]S. L. Dudarev, G. A. Botton, S. Y. Savrasov, C. J. Humphreys, and A. P. Sutton, Phys. Rev. B **57**, 1505 (1998).

[30]G. Kresse and J. Furthmüller, Phys. Rev. B **54**, 11169 (1996).

[31]G.Kresse and D. Joubert, Phys. Rev. B **59**, 1758 (1999).

[32]J. E. Medvedeva, V. I. Anisimov, M. A. Korotin, O. N. Mryasov, and A. J. Freeman, J. Phys.: Condens. Matter **12,** 4947 (2000).

[33]W. Press, *Numerical recipes 3rd edition: The art of scientific computing.* Cambridge University Press, NY, USA (2007).

[34] S. Ostanin, A. J. Craven, D. W. McComb, D. Vlacos, A. Alavi, A. T. Paxton, and M. W. Finnis, Phys. Rev. B, 65, 224109, (2002)

[35]See the FEFF documentation http://feffproject.org/feffproject-feff.html

[36]D. W. McComb, Phys. Rev. B **54**, 10 (1996)

[*] Author to whom correspondence should be addressed.E-mail:jzhu@tsinghua.edu.cn.